

Hot Deformation Characteristics of 9Cr-1.5Mo-1.25Co-VNb Ferritic-Martensitic Steel



JOONOH MOON, TAE-HO LEE, CHANG-HOON LEE, SEONG-JUN PARK,
JONG-HO SHIN, and JONG-WOOK LEE

The hot workability of 9Cr-1.5Mo-1.25Co-VNb ferritic-martensitic steel was investigated through hot compression tests using Gleeble simulator over a temperature range of 1223 K (950 °C) to 1573 K (1300 °C) and strain rates of 0.001 to 0.5 per second. Through an analysis of the stress(σ)–strain(ϵ) curves obtained during the hot compression tests, a processing map was developed to predict the hot workability, based on a dynamic material model (DMM). The processing map indicated that the hot workability deteriorates with an increase in the strain rate and a decrease in the temperature. During hot compression tests at temperatures exceeding 1473 K (1200 °C), δ -ferrite was formed along austenite grain boundaries and fine austenite grains then nucleated at the austenite/ δ -ferrite interphase due to dynamic recrystallization (DRX), which was beneficial to the hot workability. At a temperature below 1223 K (950 °C), intergranular cracking occurred, after which a transmission electron microscopy (TEM) analysis revealed that this intergranular cracking resulted from the precipitation of intergranular $M_{23}C_6$ particles.

<https://doi.org/10.1007/s11661-019-05487-4>

© The Minerals, Metals & Materials Society and ASM International 2019

I. INTRODUCTION

OWING to their excellent thermophysical properties characterized by high thermal conductivity and high creep resistance, Ferritic-Martensitic (F-M) steels with high levels of Cr (9 to 12 wt pct) have been regarded as potential candidates for use in ultra-supercritical (USC) power plants.^[1,2] F-M steels with 9 to 12 wt pct of Cr were initially developed for fossil fuel-fired power plants in the 1960s, and their creep rupture strength has gradually increased over the decades with the addition of Nb, V, and other alloying elements.^[3–5]

9 to 12 wt pct Cr steels have utilized the strengthening mechanisms of solution hardening, dislocation hardening, and precipitation hardening to improve the creep properties at high temperatures.^[5] Among the strengthening mechanisms, precipitation hardening plays a decisive role. Generally, 9 to 12 wt pct Cr steels are normalized and tempered, and their microstructures therefore typically consist of tempered martensite.^[6]

During the tempering process, Cr-enriched $M_{23}C_6$ carbides precipitate along prior austenite grain boundaries (PAGB) and martensite laths. In addition, the lath interior areas are decorated by fine MC (M: Nb and/or V) carbides that can contribute to strengthening.^[6] These precipitates impart beneficial effects on the creep properties. Previous work has reported that $M_{23}C_6$ carbides disturb the recovery of the dislocation substructure^[7] and that the MC carbides themselves obstruct the movement of dislocations, which increases the creep strength.^[8] Meanwhile, many attempts have been made to control the precipitation and coarsening behavior of these precipitates in steels because fine particles which are uniformly dispersed are the most effective means of improving the strength.^[5,9,10] Boron (B) is a typical alloying element which controls the coarsening rate of the $M_{23}C_6$ carbide; B dissolves into $M_{23}C_6$ carbides and reduces their coarsening.

As reviewed above, many works have reported beneficial effects of precipitates on the creep properties. However, a negative effect has also been reported.^[11] Heo *et al.* found that intergranular cracking under tensile stress at an elevated temperature occurred due to decohesion of the grain boundary/carbide interfaces at carbide-free grain boundaries. Thus, it is conceivable that intergranular carbide precipitation during a thermo-mechanical process, such as hot forging or hot rolling, can deteriorate the hot workability.

JOONOH MOON, TAE-HO LEE, CHANG-HOON LEE, and SEONG-JUN PARK are with the Steel Department, Metallic Materials Division, Korea Institute of Materials Science, 797 Changwondaero, Seongsangu, Changwon, Gyeongnam, 51508, Republic of Korea. Contact e-mail: mjo99@kims.re.kr JONH-HO SHIN and JONG-WOOK LEE are with Doosan Heavy Industries & Construction, 555 Gwigok-Dong, Seongsangu, Changwon, Gyeongnam, 51711, Republic of Korea.

Manuscript submitted December 27, 2018.

Article published online October 3, 2019

Recently, the modified 9Cr-1Mo steel, COST FB2, was developed in Europe, and it has received much attention owing to its excellent creep strength at higher temperatures (> 893 K (620 °C)) as compared to conventional F-M steels. However, despite their improved properties, COST FB2 steel also has potential danger of cracking in the process of forging as well as heat treatment like conventional F-M steels due to intergranular precipitation and boron segregation including boride formation.^[1] Several papers have dealt with high temperature deformation behavior of 9Cr-based F-M steels.^[12,13] They predicted the flow curves and the processing map from the compression tests at high temperature, trying to find an optimum processing condition; however, the investigation on the relationship between microstructure evolution and hot deformation behavior is not still enough.

Therefore, the goal of this study is to investigate the hot working behavior of 9Cr-1.5Mo-1.25Co-VNb F-M steel (COST FB2). To provide an optimum processing window of hot working, a processing map is developed via an analyses of the flow curves based on the dynamic material model (DMM). The correlations between the processing conditions predicted by the established processing map and the deformation microstructures are also discussed.

II. EXPERIMENTAL PROCEDURES

The chemical composition of the alloy examined is given in Table I. An ingot was initially fabricated by vacuum induction melting (VIM) and was then remelted by an electro-slag remelting (ESR) process. For homogenization, the ingot was annealed at 1523 K (1250 °C) for 5 hours, followed by air cooling. In order to investigate the hot working behavior during the forging process, the hot compression tests were carried out using a Gleeble simulator (Gleeble 3500, Dynamic System Inc.). Figure 1 shows an equilibrium phase diagram of the tested alloys as calculated by Thermo-calc. software (TCFE 7 database). Here, hot compression tests were carried out above the A_{e3} temperature, as calculated in Figure 1.

The detailed schedule of hot compression tests is presented schematically in Figure 2. The specimens were heated to a temperature range of 1223 K (950 °C) to 1573 K (1300 °C) and the hot compression tests were then carried out.

Table I. Chemical Composition of the Tested Sample (in wt pct) (Balance Fe)

C	Cr	Mn	Mo	V	Co	Nb	B, ppm	N, ppm
0.12	9.0	0.4	1.5	0.2	1.2	0.05	80 to 110	150 to 300

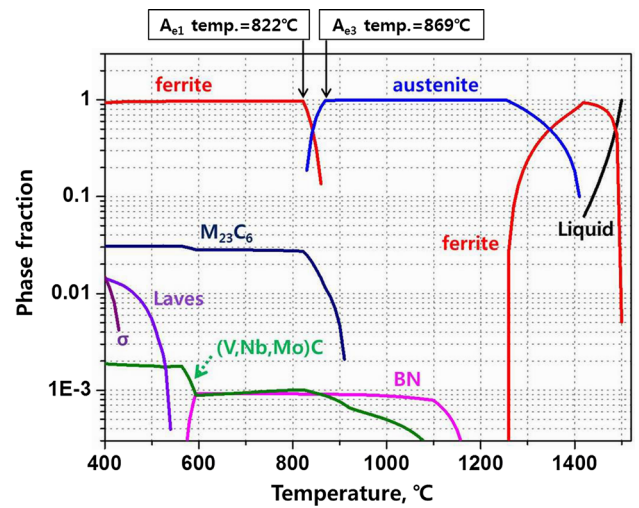


Fig. 1—Equilibrium phase fraction of the tested alloy as calculated by Thermo-Calc.

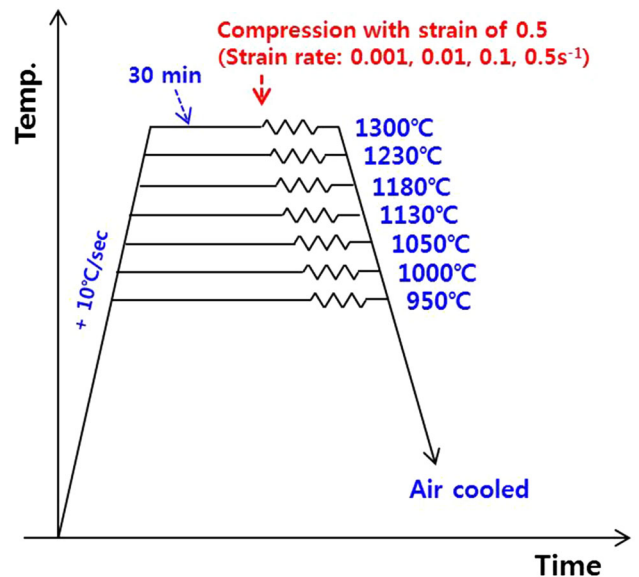


Fig. 2—Schematic diagram of hot compression test.

Through an analysis of the flow curves obtained from the hot compression tests, a processing map was developed based on the dynamic material model (DMM), and the hot workability was predicted by the processing map. After the hot compression tests, the samples were etched with a mixed solution of 5 mL of hydrochloric acid, 1 g of picric acid, and 100 mL of ethanol, with the microstructures then observed by optical microscopy (OM, EPIPHOT, Nikon), scanning electron microscopy (SEM, JSM-7001F, JEOL), and transmission electron microscopy (TEM, JEM2100F, JEOL). The particles in the samples were identified using transmission electron microscopy (TEM, JEM2100F,

JEOL) after twin-jet electrolytic polishing with a mixed solution of 10 pct perchloric acid and 90 pct methanol at 248 K (− 25 °C).

III. RESULTS AND DISCUSSION

A. Hot Compression Test

Figure 3 shows the optical micrograph of a solution-treated sample, indicating that the microstructure consisted of martensite and some amount of δ -ferrite.

According to the phase diagram in Figure 1, δ -ferrite begins to form at temperature above approximately 1473 K (1200 °C), while the δ -ferrite in Figure 3 may have formed during the solution treatment at 1523 K (1250 °C). An austenite-to-martensite transformation during air cooling will occur due to high hardenability of a tested sample.^[14] Xu *et al.*^[14] investigated the phase transformation behavior of 9Cr ferritic steel, which has a composition similar to that of our sample, and reported that the austenite-to-martensite transformation took place during continuous cooling.

Figure 4 shows the flow curves obtained from hot compression tests carried out following the schedule presented in Figure 2.

The flow stress increased with an increase in the strain rate and a decrease in the temperature. As shown in Figure 4, softening of the material occurred during hot deformation at temperatures exceeding 1403 K (1130 °C); *i.e.*, the flow curves exhibited initial strain hardening before reaching the point of peak stress, followed by a decrease in the stress. This softening phenomenon also remarkably occurs in flow curves obtained from compression tests under a low strain rate. In the literature,^[13,15–26] it has been reported that dynamic recrystallization (DRX) behavior leads to softening during deformation. Therefore, it is conceivable that the softening behavior in Figure 4 resulted from DRX.

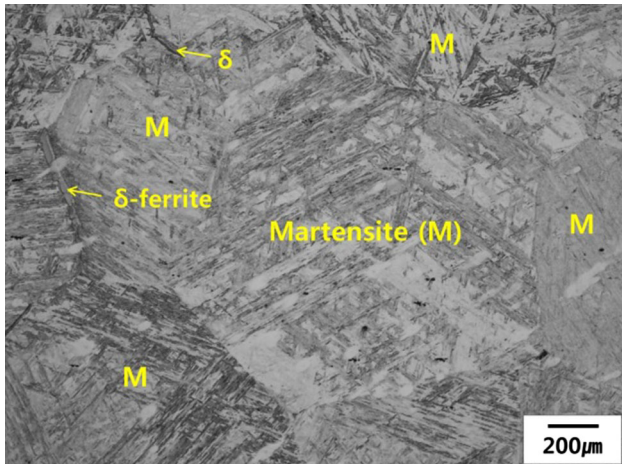


Fig. 3—Optical micrograph after the solution treatment (M.: Martensite, δ .: δ ferrite).

B. Processing Map

Recently, many studies have used a processing map for predictions of the hot workability.^[13,15,23,27,28] A processing map can be developed based on a dynamic material model (DMM), with the DMM then used to consider the deformation applied to the material as a dissipative power element.^[29] That is, the total dissipated power (P) absorbed by the sample can be divided into the two complementary parts of J and G , where J and G indicate the power dissipation by a microstructural evolution process, such as DRX and dynamic recovery (DRV), and the plastic deformation, respectively.^[29] Here, the total power can be determined as follows:

$$P = \sigma \dot{\epsilon} = J + G = \int_0^{\sigma} \dot{\epsilon} d\sigma + \int_0^{\dot{\epsilon}} \sigma d\dot{\epsilon} \quad [1]$$

where σ is the flow stress and $\dot{\epsilon}$ is the strain rate under the given strain condition. The flow stress at the given temperature can be expressed by Eq. [2]:

$$\sigma = K\dot{\epsilon}^m \quad [2]$$

In this equation, K is a constant and m is the strain rate sensitivity parameter. The strain rate sensitivity parameter is determined by power partitioning and is calculated by Eq. [3]:

$$m = \frac{dJ}{dG} = \frac{\dot{\epsilon} d\sigma}{\sigma d\dot{\epsilon}} = \left(\frac{d\sigma}{\sigma} \right) / \left(\frac{d\dot{\epsilon}}{\dot{\epsilon}} \right) = \frac{d \ln \sigma}{d \ln \dot{\epsilon}} \quad [3]$$

In Eq. [1], J can be solved as follows:

$$J = \int_0^{\sigma} \dot{\epsilon} d\sigma = \int_0^{\dot{\epsilon}} m\sigma d\dot{\epsilon} = mG = \frac{m\sigma\dot{\epsilon}}{1+m} \quad [4]$$

The efficiency of the power dissipation, η , is calculated by Eq. [5]; ideal power dissipation (J_{\max}) would then occur when $m = 1.0$.^[19]

$$\eta = \frac{J}{J_{\max}} = \left(\frac{m\sigma\dot{\epsilon}}{1+m} \right) / \left(\frac{\sigma\dot{\epsilon}}{2} \right) = \frac{2m}{1+m} \quad [5]$$

The power dissipation value indicates the effect of the microstructural evolution process, such as DRX and DRV, on the hot workability; however, this cannot sufficiently define safe and unsafe deformation conditions. Prasad^[30] introduced the instability criterion (ζ) for hot deformation from DMM in the form of the following equation:

$$\zeta = \frac{d \ln(m/(1+m))}{d \ln \dot{\epsilon}} + m < 0 \quad [6]$$

In Eq. [6], a negative value of ζ implies that the material undergoes unstable plastic deformation. In this study, η and ζ values were calculated under different

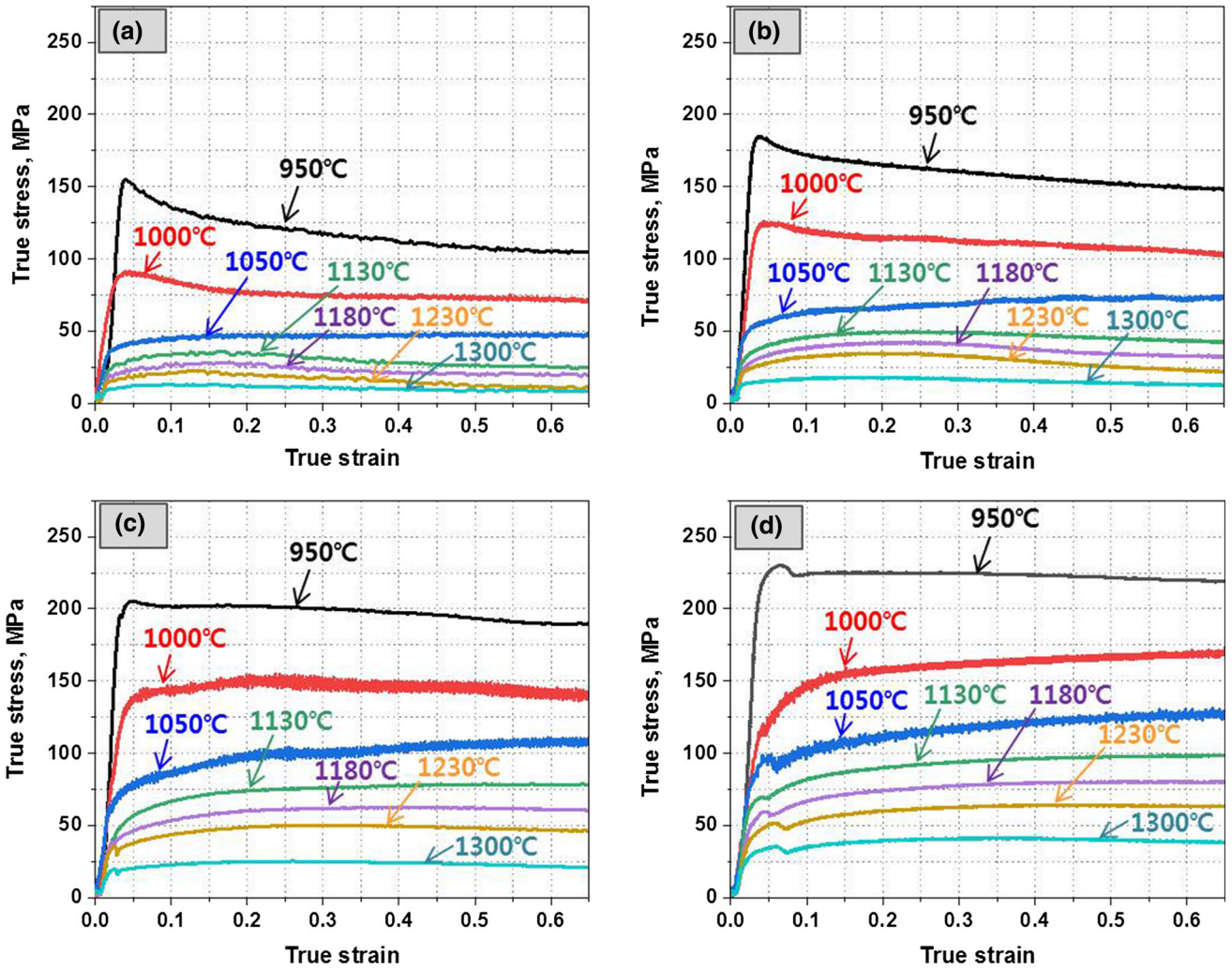


Fig. 4—True stress–strain curves obtained from compression tests at strain rates of (a) 0.001 s^{-1} , (b) 0.01 s^{-1} , (c) 0.1 s^{-1} , and (d) 0.5 s^{-1} .

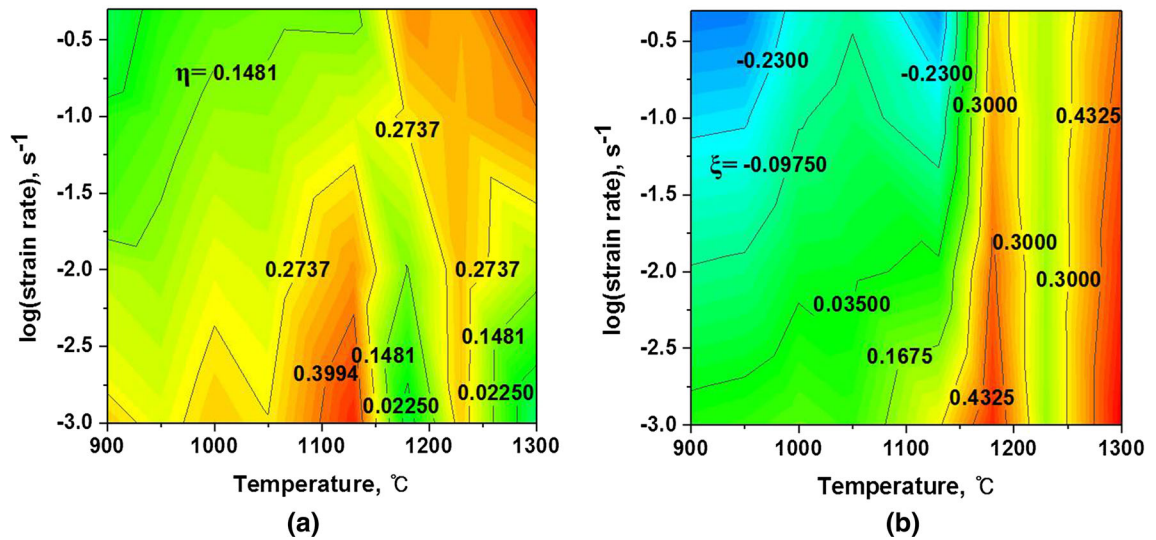


Fig. 5—(a) Efficiency of the power dissipation and (b) instability map obtained at a strain of 0.5 during the compression test.

deformation conditions using the flow stress data in Figure 4 and the efficiency rates of the power dissipation map and instability map were plotted using Eqs. [5] and [6], as shown in Figure 5.

In Figure 5(b), the negative contour numbers refer to unsafe regions for hot deformation. The instability map in Figure 5(b) indicates that the hot workability became worse with an increase in the strain rate and a decrease in the temperature.

C. Effects of Microstructural Features on the Hot Deformation

Figure 6(a) shows an optical micrograph of a specimen which deformed at 1573 K (1300 °C) at a strain rate of 0.1 s^{-1} .

In Figure 6(a), the microstructure shows a ‘necklace’ structure, *i.e.*, new equiaxed recrystallized grains surrounding the δ -ferrite due to dynamic recrystallization (DRX). The formation process of the necklace structure is schematically summarized in Figure 7. First, martensite was transformed into austenite during the heating up to 1573 K (1300 °C), after which some δ -ferrite began to form along the austenite grain boundaries when holding the temperature at 1573 K (1300 °C) for 30 min. The phase diagram in Figure 1 indicates that δ -ferrite can nucleate at 1573 K (1300 °C). Next, equiaxed austenite was recrystallized around δ -ferrite at the austenite/ δ -ferrite interphase due to DRX during the compression test with up to 50 pct strain, as shown in Figure 7(d). Finally, the primary and recrystallized

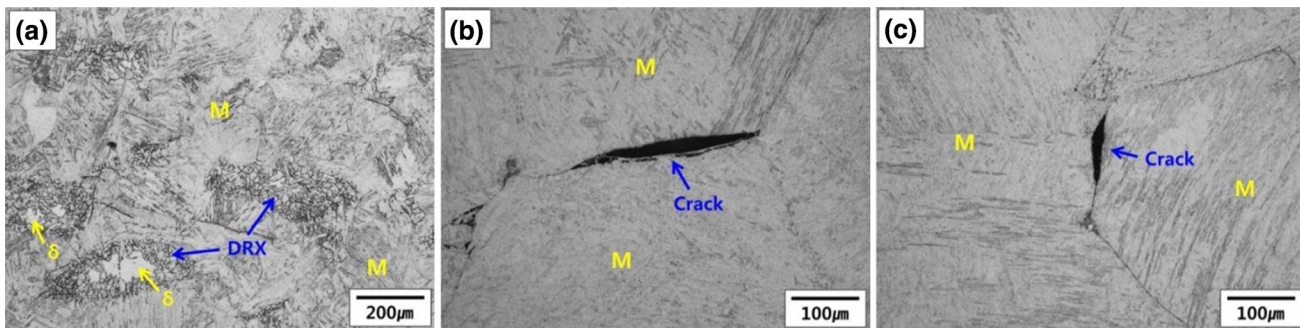


Fig. 6—Optical micrographs of the samples after compression tests at (a) 1573 K (1300 °C) at a strain rate of 0.1 s^{-1} , (b) 1223 K (950 °C) at a strain rate of 0.01 s^{-1} , and (c) 1223 K (950 °C) at a strain rate of 0.1 s^{-1} .

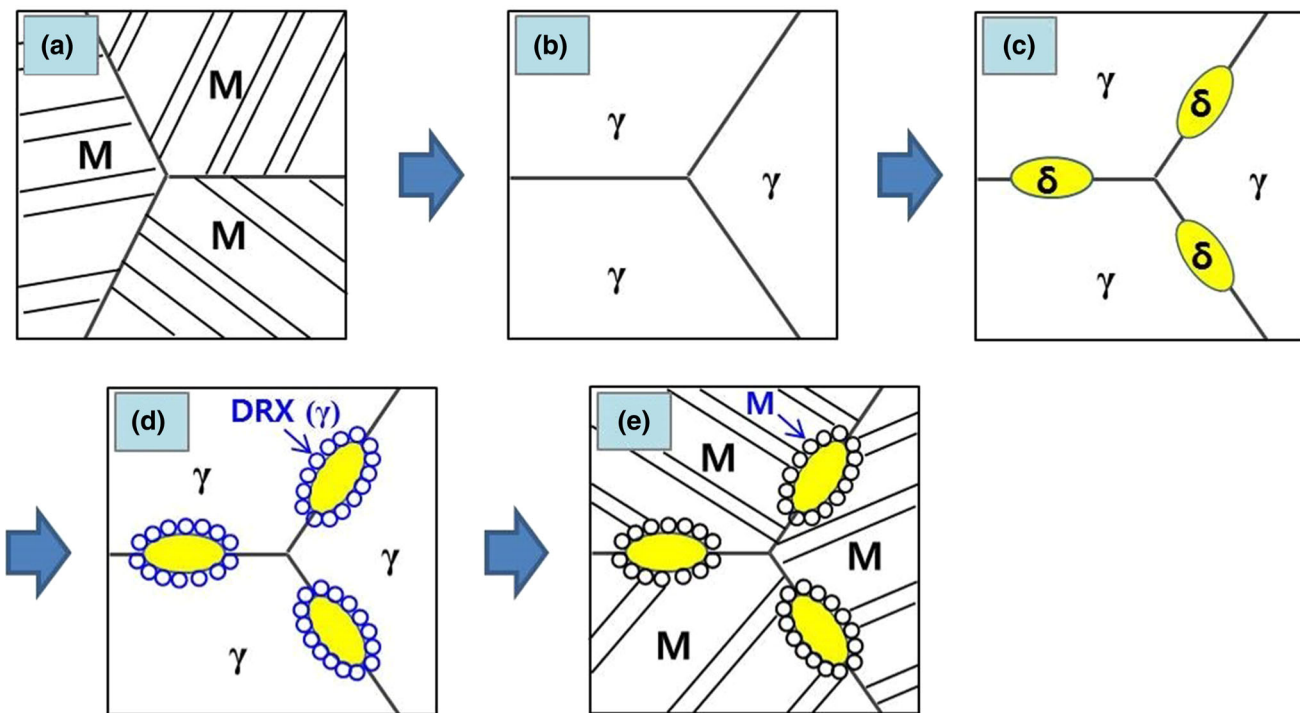


Fig. 7—Schematic illustration of the microstructural evolution during the compression test at 1573 K (1300 °C): (a) as solution-treated, (b) heating up to 1573 K (1300 °C), (c) holding at 1573 K (1300 °C) for 30 min, (d) hot compression test up to 50 pct strain, and (e) cooled to room temperature.

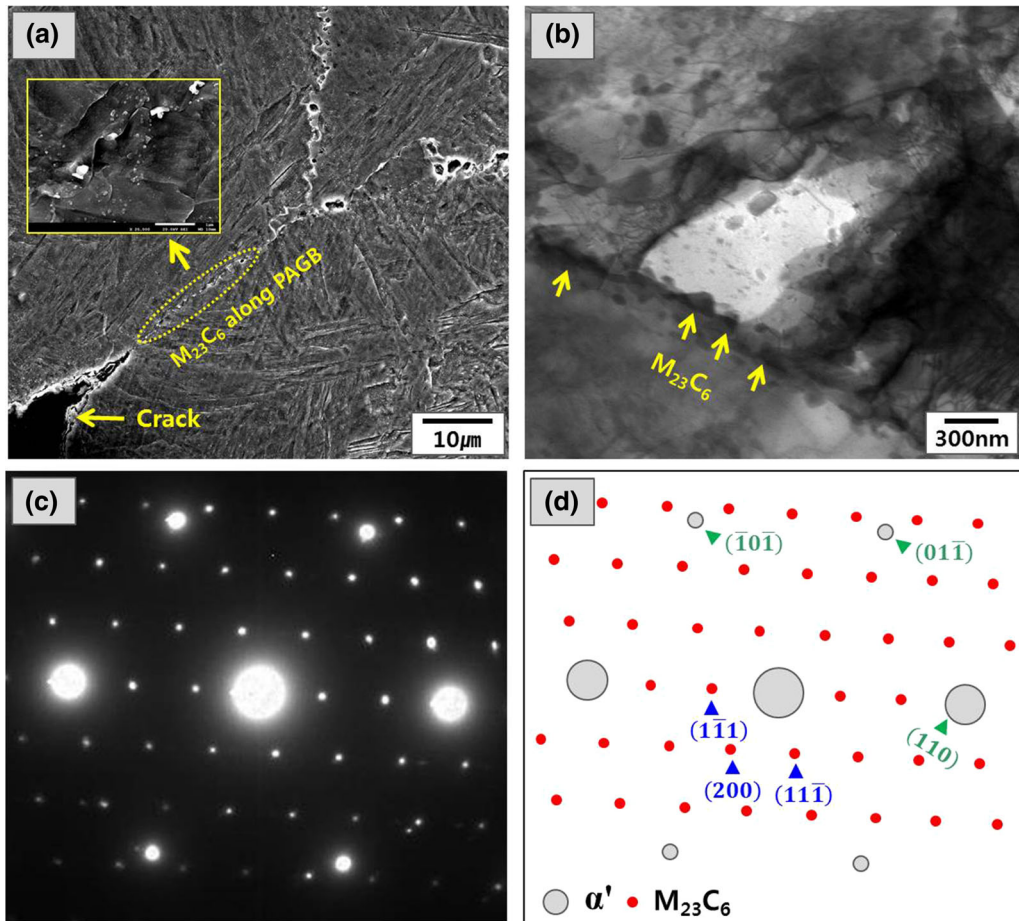


Fig. 8—(a) SEM micrograph showing $M_{23}C_6$ particles along the prior austenite grain boundaries (PAGB), (b) TEM micrograph of a $M_{23}C_6$ particle, (c) SAD pattern ($z = [\bar{1}11]_z // [\bar{1}10]_{M_{23}C_6}$), and (d) a computer-simulated SAD pattern.

austenite was transformed into martensite during the cooling process.

Previous work^[31,32] indicated that DRX helped a stable hot deformation. Xi *et al.*^[31] investigated the hot deformation behavior of a Cu-bearing 317LN stainless steel and reported that the stable deformation at high temperature occurred with an accompanying DRX. Zafarhandi *et al.*^[32] studied the hot tensile deformation behavior of cast and homogenized Haynes 25 Co-Cr-W-Ni alloy and indicated that the formation of new grains by DRX reduced the deformation energy and postpones the formation of voids and final fracture, leading to the improvement of total elongation. According to the processing map in Figure 5, the positive instability parameter, corresponding to the safe deformation condition, was predicted under the condition of 1573 K (1300 °C) and then DRX behavior shown in Figures 6(a) and 7 must have contributed to the safe deformation at 1573K (1300 °C).

Figures 6(b) and (c) show optical micrographs of a specimen which deformed at 1223 K (950 °C) with strain rates of 0.01 and 0.1 s^{-1} . Cracking occurred along the PAGB, and these results match the predictions by the processing map well, as shown in Figure 5. That is, under the condition of 1223 K (950 °C) at strain rates of 0.1 and 0.01 s^{-1} , the negative instability parameter was

predicted, corresponding to an unsafe deformation condition for hot working. This led to cracking, as shown in Figures 6(b) and (c). To reveal the origin of the intergranular cracking, we carried out a microstructural analysis using SEM and TEM, as shown in Figure 8. It was found that the intergranular precipitation of $M_{23}C_6$ carbides played an important role in the formation of cracks.

Figure 8(a) presents a SEM micrograph showing particles which existed at the front end of a crack along the PAGB. A closer examination using TEM-SAD (Selected Area Diffraction) identified them as $M_{23}C_6$ following the Kurdjumov–Sachs orientation relationship with a martensite matrix.^[33]

$$[\bar{1}11]_z // [\bar{1}11]_{M_{23}C_6} \text{ and } (110)_z // (\bar{1}\bar{1}\bar{1})_{M_{23}C_6}$$

The result of the phase diagram calculation also indicated that $M_{23}C_6$ carbides can precipitate at temperatures above 1173 K (900 °C). Previous work^[15,34] pointed out that intergranular precipitates made grain boundaries brittle, leading to brittle intergranular fractures. Therefore, the intergranular cracks which occurred during the hot compression tests, as shown in Figs. 6(b) and (c), may have occurred due to

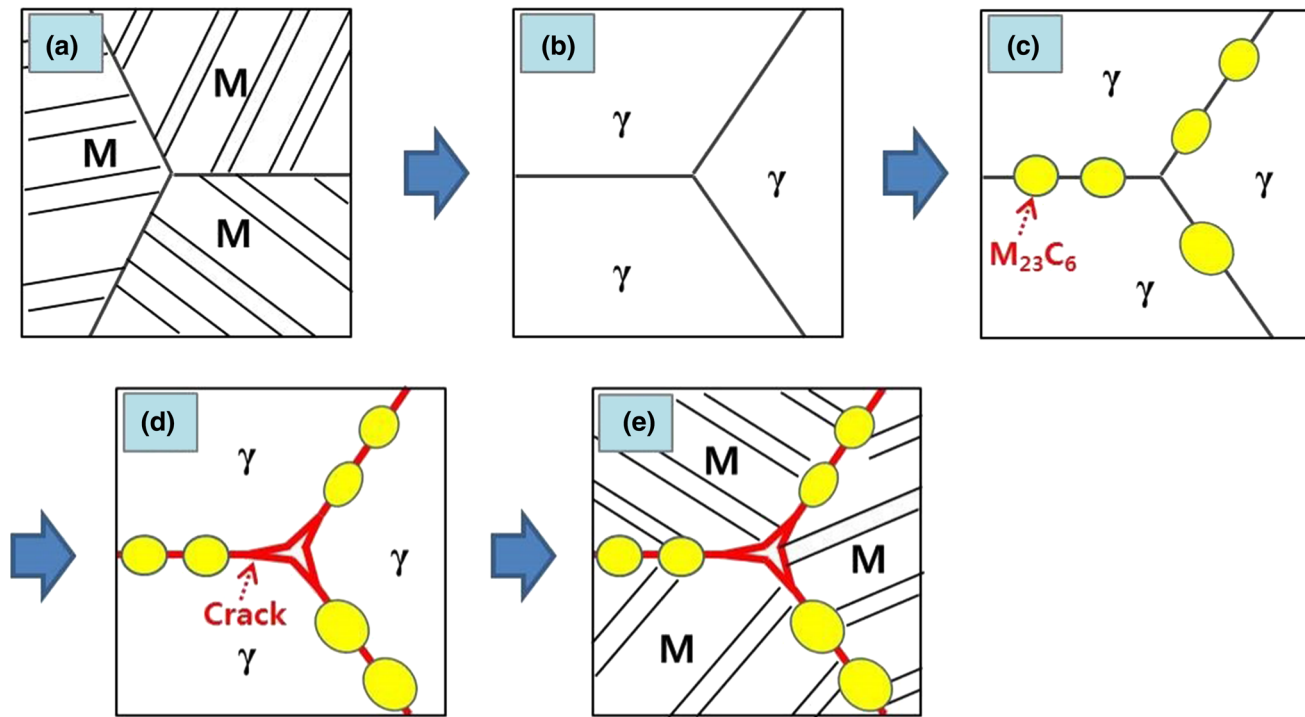


Fig. 9—Schematic illustration of the microstructural evolution during the compression test at 1223 K (950 °C): (a) as solution-treated, (b) heating up to 1223 K (950 °C), (c) holding at 1223 K (950 °C) for 30 min, (d) hot compression test up to 50 pct strain, and (e) cooled to room temperature.

intergranular $M_{23}C_6$ precipitation. The mechanism of the decrease in the hot workability by the precipitation of $M_{23}C_6$ carbides along the PAGB is schematically summarized in Figure 9. Martensite was initially transformed into austenite during the heating step to 1223 K (950 °C), after which $M_{23}C_6$ carbides precipitated along the austenite grain boundaries as the temperature was held at 1223 K (950 °C) for 30 minutes. Subsequent compressive stress led to intergranular cracking, as shown in Figure 9(d). Afterward, austenite was transformed into martensite during the cooling process.

IV. CONCLUDING REMARKS

The hot workability of 9Cr-1.5Mo-1.25Co-VNb ferritic-martensitic steel was investigated, and the following results were drawn.

- (1) In order to predict the hot workability, a processing map was established through hot compression tests based on the DMM. The developed instability map predicts the safe and unsafe hot working domains, and the reliability of the instability map was proved by a microstructure analysis of specimens deformed under unsafe conditions.
- (2) During hot compression tests at temperature exceeding 1473 K (1200 °C), δ -ferrite initially formed along the austenite grain boundaries, after which fine austenite grains nucleated; thus, surrounding the δ -ferrite due to dynamic

recrystallization (DRX), *via* what is known as ‘necklace microstructure’. This DRX phenomenon contributed to stable hot deformation.

- (3) Intergranular cracking occurred during the hot compression test at 1223 K (950 °C), and this result was in good agreement with the prediction result by the instability map. SEM and TEM observations clearly demonstrated that this intergranular cracking was caused by intergranular $M_{23}C_6$ precipitation.

ACKNOWLEDGMENTS

J. Moon was supported financially by Doosan Heavy Industries & Construction of Republic of Korea. J. Moon was also supported financially by the Fundamental Research Program of the Korea Institute of Materials Science (KIMS) (POC3380 & PNK6500).

REFERENCES

1. F. Liu, D.H.R. Fors, A. Golpayegani, G.-O. Andrén, and G. Wahmström: *Metall. Trans. A*, 2012, vol. 43A, pp. 4053–62.
2. Z.B. Zhang, O.V. Mishin, N.R. Tao, and W. Pantleon: *J. Nucl. Mater.*, 2015, vol. 458, pp. 64–69.
3. T. Shrestha, M. Basirat, I. Charit, G.P. Potirniche, K.K. Rink, and U. Sahaym: *J. Nucl. Mater.*, 2012, vol. 423, pp. 110–19.
4. M. Shibuya, Y. Toda, K. Sawada, H. Kushima, and K. Kimura: *Mater. Sci. & Eng. A*, 2016, vol. 652, pp. 1–6.

5. F.-S. Yin, W.-S. Jung, and S.-H. Chung: *Scripta Mater*, 2007, vol. 57, pp. 469–472.
6. J. Moon, C.-H. Lee, T.-H. Lee, M.-H. Jang, M.-G. Park, and H.N. Han: *J. Nucl. Mater.*, 2014, vol. 455, pp. 81–85.
7. K. Iwanaga, T. Tsuchiyama, and S. Takaki: *Key Eng. Mater.*, 2000, vols. 171–174, pp. 477–82.
8. H. Cerjak, P. Hofer, and B. Schaffernak: *Key Eng. Mater.*, 2000, vols. 171–174, pp. 453–60.
9. J.F. Mansfield: *J. Mater. Sci.*, 1987, vol. 22, pp. 1277–85.
10. K. Maruyama, K. Sawada, and J.-I. Koike: *ISIJ Int.*, 2001, vol. 41, pp. 641–53.
11. N.H. Heo, J.C. Chang, K.B. Yoo, J.K. Lee, and J. Kim: *Mater. Sci. Eng. A*, 2011, vol. 528, pp. 2678–85.
12. S.A. Krishnan, C. Phaniraj, C. Ravishankar, A.K. Bhaduri, and P.V. Sivaprasad: *Inter. J. Press. Ves. Piping*, 2011, vol. 88, pp. 501–506.
13. G. Zhang, Z. Zhou, H. Sun, L. Zou, M. Wang, and S. Li: *J. Nucl. Mater.*, 2014, vol. 455, pp. 139–44.
14. L. Xu, Z. Yan, Y. Liu, H. Li, B. Ning, and Z. Qiao: *J. Mater. Res.*, 2013, vol. 28, pp. 2835–43.
15. J. Moon, T.-H. Lee, J.-H. Shin, and J.-W. Lee: *Mater. Sci. & Eng. A*, 2014, vol. 594, pp. 302–308.
16. M. Ma, H. Ding, Z.-Y. Tang, J.-W. Zhao, Z.-H. Jiang, and G.-W. Fan: *J. Iron. Steel Res. Int.*, 2016, vol. 23, pp. 244–52.
17. E.I. Poliak and J.J. Jonas: *Acta Mater.*, 1996, vol. 44, pp. 127–36.
18. S. Saadatkia, H. Mirzadeh, and J.-M. Cabrera: *Mater. Sci. & Eng. A*, 2015, vol. 636, pp. 196–202.
19. E.I. Poliak and J.J. Jonas: *ISIJ Int.*, 2003, vol. 43, pp. 684–91.
20. H. Mirzadeh, J.M. Cabrera, A. Najafizadeh, and P.R. Calvillo: *Mater. Sci. & Eng. A*, 2012, vol. 538, pp. 236–45.
21. H. Mirzadeh, J.M. Cabrera, J.M. Prado, and A. Najafizadeh: *Mater. Sci. & Eng. A*, 2011, vol. 528, pp. 3876–82.
22. H. Mirzadeh and A. Najafizadeh: *Mater. Des.*, 2010, vol. 31, pp. 1174–79.
23. S.M. Abbasi and A. Momeni: *Mater. Sci. & Eng. A*, 2012, vol. 552, pp. 330–35.
24. M. Mirzaee, H. Keshmiri, G.R. Ebrahimi, and A. Momeni: *Sci. & Eng. A*, 2012, vol. 551, pp. 25–31.
25. A. Momeni and K. Dehghani: *Metall. Trans. A*, 2011, vol. 42A, pp. 1925–32.
26. A. Momeni, K. Dehghani, G.R. Ebrahimi, and H. Keshmiri: *Metall. Trans. A*, 2011, vol. 41A, pp. 2898–2904.
27. Y.L. Fang, Z.Y. Liu, H.M. Song, and L.Z. Jiang: *Mater. Sci. & Eng. A*, 2009, vol. 526, pp. 128–33.
28. S. Venugopal, S.L. Mannan, and Y.V.R.K. Prasad: *Mater. Lett.*, 1992, vol. 15, pp. 79–83.
29. Y. Wu, M. Zhang, X. Xie, J. Dong, F. Liu, and S. Zhao: *J. Alloys Compd.*, 2016, vol. 656, pp. 119–31.
30. Y.V.R.K. Prasad: *Indian J. Technol.*, 1990, vol. 28, pp. 435–51.
31. T. Xi, C. Yang, M.B. Shahzad, and K. Yang: *Mater. Des.*, 2015, vol. 87, pp. 303–12.
32. M.S. Zafarghandi, S.M. Abbasi, and A. Momeni: *J. Alloys Compd.*, 2019, vol. 774, pp. 18–29.
33. A. Kipelova, A. Belyakov, and R. Kaibyshev: *Philos. Mag.*, 2013, vol. 93, pp. 2259–68.
34. J.F. Grubb and R.N. Wright: *Metall. Trans. A*, 1979, vol. 10A, pp. 1247–55.

Publisher's Note Springer Nature remains neutral with regard to jurisdictional claims in published maps and institutional affiliations.